Metal Nanoparticles of Complex Morphologies
Bottom-Up Synthesis to Applications

Editors: Tapan K. Sau & Andrey L. Rogach

Chapter 6

"Size- and Shape-Variant Magnetic Nanoparticles: Synthesis and Characterisation for Biomedical Applications"

Kristen Stojak, Hariharan Srikanth, and Manh-Huong Phan*
*Department of Physics, Functional Materials Laboratory, University of South Florida, 4202 East Fowler Avenue, Tampa, Florida 33647, USA *E-mail: phanm@usf.edu*

Nguyen T. K. Thanh*
*Department of Physics & Astronomy, University College London, Gower Street, London WC1E 6BT, UK. The Davy-Faraday Research Laboratory, The Royal Institution of Great Britain, 21 Albemarle Street, London, W1S 4BS, UK *E-mail: ntk.thanh@ucl.ac.uk*

Table of Contents

1. Introduction

Magnetic nanoparticles (MNPs) have found wide applications in biomedicine due to their magnetic properties and dimensions being smaller than or comparable to several biological entities such as cells (10-100 μm), viruses (20-450 nm), and proteins (5-50 nm) [1-3]. The ability of these MNPs to be manipulated by an external magnetic field make them especially attractive for localized treatment options such as targeted drug delivery and hyperthermia, as well as diagnostics like enhancing contrast in existing magnetic resonance imaging (MRI) techniques and sensors based on the detection of a magnetic signal [4,5]. In most cases, the MNPs are required to be monodisperse so that each individual MNP has nearly identical physical and chemical properties for controlled biodistribution, and bioelimination [3,6]. As magnetic labels, the MNPs should be superparamagnetic to have zero magnetic remanence in the absence of an external magnetic field and are also required to have high magnetization [5]. This is why different synthetic approaches have been developed to achieve these goals [3,6-12]. Recently, particular attention has been paid to growth of shape-variant MNPs which, could be used for more novel biomedical applications. For example, they could have utility in biomedical immune-electron microscopy allowing differentiation by both size and shape simultaneously [13-15]. It is important to note that MNPs with tunable shapes and sizes provide more magnetic labeling options that are currently restricted to spherical MNPs below 15 nm in size [13]. Once shape-variant MNPs are used, different biological molecules (eg: proteins, lipids) can be labeled to simultaneously target different sites within a single sample, giving a direct comparison of signaling networks or multi-subunit molecular machines.

This book chapter will serve as a guide and review of currently available chemical methods for synthetic of MNPs shape and size and their characterisation. It will also provide the reader with a comprehensive understanding of magnetism in these synthesized MNPs and some useful biomedical applications.

2. Synthetic of size- and shape-variant ferrite nanoparticles

Ferrites are very exciting for biomedical use. Magnetite (Fe_3O_4), a ferrite, has been approved by the FDA for medical use in a variety of applications. The synthetic method for making ferrite MNPs can drastically change their physical properties, such as size, shape, and magnetism. The synthetic technique used to make ferrite MNPs also determines how the surface is coated to allow for suspension in different solvents such as hexane, water and saline solutions.

There are a wide variety of synthetic techniques available for making ferrite MNPs. The more common techniques are bottom-up approaches, meaning that reagents are broken down and MNPs are built up from agglomerations of atoms. Four promising synthetic methods for shape and size variation are:

- Thermal decomposition
- Co-precipitation
- Solvothermal
- Microemulsion

This section will give a brief description of each, followed by which parameters affect the size and shape of the MNPs.

2.1 Thermal decomposition

Thermal decomposition is a very common synthetic technique for making ferrite MNPs due to the quality of the resulting MNPs and the speed of the reaction [9,16-23]. As the name *thermal decomposition* implies, this technique takes advantage of materials breaking down and forming new compositions at various temperatures. This technique is particularly useful for making very small, uniform nanocrystals. The basic procedure [9] is to mix organometallic compounds with a surfactant to stabilize the particles in a high boiling point organic solvent. The organometallic materials are generally metal acetylacetonates [M(acac)$_n$, M = Fe, Mn, Co, Ni, Cr, n = 2, 3], metal cupferronates [M$_x$Cup$_x$, M = metal ion, Cup = N-nitrosophenylhydroxylamine], or carbonyls. The surfactant, or surface active agent, is used as a stabilizing coating for the MNPs. The surfactant determines what types of solvent the MNPs can be well dispersed in, and prevents them from further oxidation. Fatty acids such as oleic acid, hexadecylamine and oleylamine are common surfactants for this technique [16]. Benzyl ether, phenyl ether, octyl ether, or 1-octadecene can be used as the high boiling point organic solvents. Generally there is also use of an alcohol as a cosurfactant. Some commonly used alcohols are 1,2-hexadecanediol, 1,2-tetradecanediol, or 1,2-dodecanediol. Figure 6.1 shows how the various reagents come together to create a ferrite MNP.

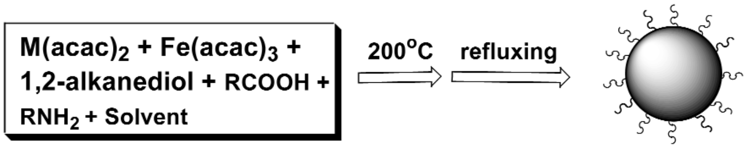

Fig. 6.1. Flow chart shows how to create inverse spinel MNPs using a thermal decomposition method with an oleate coating. The reagents are as follows: Fe(acac)$_3$, iron (III) acetylacetonate, as an organometallic material; ROH, a hydroxyl, with 1,2-hexadecanediol as an example; RCOOH as a carboxyl, with oleic acid as an example; RNH$_2$ as an amine, with oleylamine as an example and a solvent. The phase of the resulting MNP would be MFe$_2$O$_4$ with "M" standing for "metal." Reprinted with permission from Ref. ***[16].***

An example of a synthetic procedure for thermal decomposition is as follows. First, all reagents are mixed together in one flask; this includes all organometallic materials, surfactants, alcohols, and solvents. After mixing, oxygen is purged from the flask and heating is commenced. The flask is heated to a temperature, where the precursor will decompose and the MNPs are formed. After a short period of time, the reaction is stopped by removing the heat source. One of the advantages to using thermal decomposition is that it is considered a *one-pot synthesis* meaning that multiple chemical reactions occur in one reaction flask.

Once this part of the synthesis is complete, the sample is centrifuged several times in the presence of ethanol to wash the MNPs and remove any excess chemicals from the synthesis. Lack of suspension in the final solvent is indicative of MNPs with an insufficient surfactant coating, so it is vital to remove these particles. The final result of ferrite MNPs, such as magnetite or cobalt ferrite, in a non-polar solvent is a ferrofluid.

2.1.1 Surface functionalization

MNPs synthesized by this method are excellent for dispersing in non-polar solvents such as toluene or hexane, but will not suspend in polar solvents such as water or phosphate buffered saline (PBS) solutions, which is essential for biomedical use. For this reason, these MNPs need to be *surface functionalized* with a bio-compatible material before suspension in water or PBS and injection into a living entity [9, 17-21]. There are two basic types of surface functionalization: one where the initial coating is removed and replaced by a bio-compatible coating, and another where the bio-compatible coating is added on top of the original coating.

Both types of surface functionalization described above are called *ligand exchange*, which is also commonly referred to as *surface exchange*. Ligand exchange builds upon the initial coating. In this method, the MNPs are prepared with their oleate coating and suspended in hexane. An aqueous mixture of a bio-compatible agent, such as α-cyclodextrin or dimercaptosuccinic acid [18], is created and the two solutions are mixed together. After they are left stirring for a period of time, the MNPs’ coatings are exchanged from the oleate coating to the α-cyclodextrin coating, as indicated by visible suspension in the aqueous solution [19]. The two solvent mixtures are then separated and the MNPs have been surface functionalized. Figure 6.2 shows the surface exchange method and resulting MNP solutions.

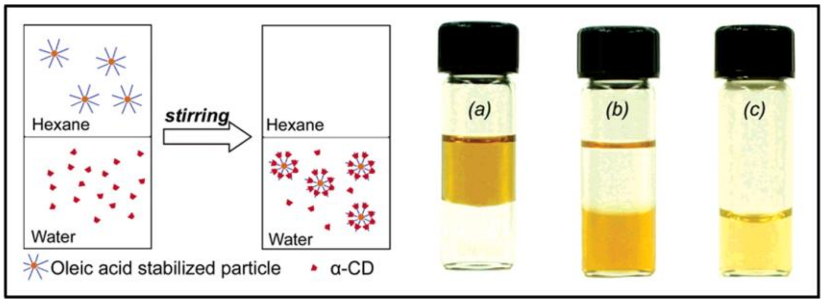

Fig. 6.2. On the left is a schematic of how the surface exchange method uses the oleate coating to attach MNPs to α-cyclodextrin. On the right are actual MNP solutions-(a) shows the MNPs suspended in hexane with the aqueous α-cyclodextrin solution below it; (b) shows the MNPs have settled in to the aqueous α-cyclodextrin solution after stirring for ~24 hours and the empty hexane; (c) shows the final product of α-cyclodextrin coated magnetite MNPs suspended in water. Reprinted with permission from Ref. [19]: Y. Wang, J. F. Wong, X. Teng, X. Z. Lin, and H. Yang, *Nano Letters* **2003**, *3*, 1555. Copyright 2011 American Chemical Society.

Figure 6.3 shows another version of ligand exchange. With this method, the original coating is stripped from the MNPs and a new, bio-compatible coating replaces the old one [20].

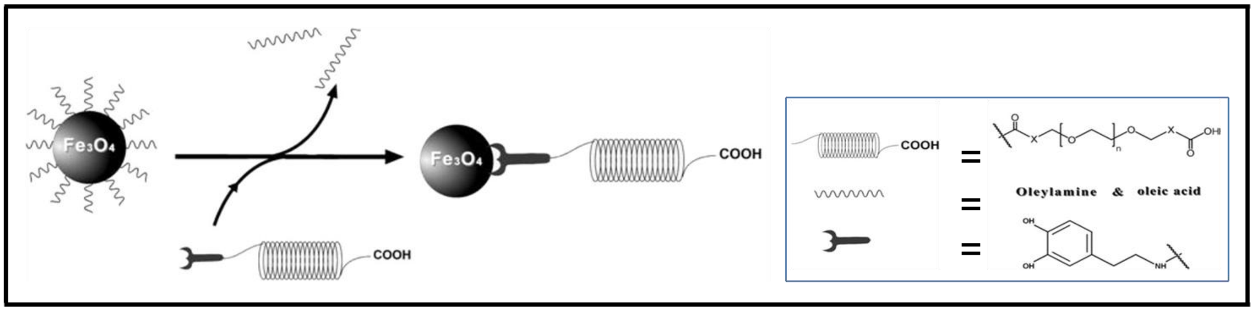

Fig. 6.3. This diagram shows how ligand exchange works as a means of surface functionalization by stripping the MNP of its original coating and replacing it with one that suspends in a polar solution. Reprinted with permission from Ref. [20].

Another method that builds upon the oleate coating involves the *intercalation of surfactants* [21]. In this method, the MNPs start with any type of hydrophobic coating, and an *amphiphilic* polymer is added to the surface. The amphiphilic polymer would have affinity with both the lipids coating the MNP and the water in the aqueous solution, however the polymer chains must be long enough to coat the entire particle, or else exposure of the original coating may be present. For this reason, an additional molecule must be added to cross-link the polymer chains, thus creating a robust shell for the MNPs. Figure 6.3 shows how this process works. In one example of this procedure, the MNPs and the polymer are separately suspended in chloroform and the two solutions are mixed together. After stirring for a period of time, the chloroform is allowed to dry and a separate chloroform solution containing the cross-linking material is added to the dry mixture. After sonicating, the solvent is evaporated a second time and the MNPs are suspended in a buffer solution, which is then filtered to remove any unbound polymer. The resulting MNPs suspend in water and remain stable for several months.

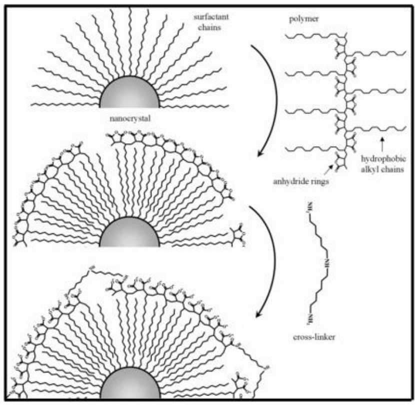

Fig. 6.4. This diagram shows how a polymer is attached and then cross-linked on the surface of an initially oleate-coated MNP. Reprinted with permission from Ref. [21]: T. Pellegrino, L. Manna, S. Kudera, T. Liedl, D. Kiktysh, A. L. Rogach, S. Keller, J. Radler, G. Natile, and W. J. Parak, *Nano Letters* **2004**, *4*, 703. Copyright 2011 American Chemical Society.

Other common bio-compatible coatings for MNPs include silica, gold, polyvinyl alcohol (PVA), and polyethylene glycol (PEG) [9].

2.1.2 Synthesis of Shape and size variant MNPs

By changing the amount of surfactants and solvents or by altering their ratios with the thermal decomposition synthetic method, an experimenter can obtain particles of vastly different morphologies. The size, shape and uniformity can be greatly altered and these parameters can be finely tuned.

Several research groups have observed that when there is a high solvent to metal precursor concentration ratio, very small, uniform MNPs form. This is attributed to the fact that as the amount of solvent within a solution is increased; the decomposed metals take up a smaller and smaller percentage of the overall solution. Thus forming smaller clusters of material and resulting in smaller MNPs. However, it has been reported that below or above a certain amount of surfactant, the amount of solvent becomes unimportant [16, 23]. In addition to the amount of solvent and surfactant in the solution, the length of the alcohol chain also plays a role in the size of the resulting MNPs. A longer chain, such as a hexadecanediol, yields smaller particles than alcohols with shorter chains such as tetra- and do-decanediols. Table 6.1 shows the correlation of resulting magnetite MNP size with alcohol chain length, amount of surfactant, and amount and *type* of solvent present in the reaction.

Table 6.1. Using 2 mmol of iron (III) acetylacetonate as the metal salt and systematically changing amounts and types of all other reactants yields a variety of particle sizes for magnetite MNPs [16].

Particle Size (nm)	1,2-hexadecanediol (mmol)	1,2-tetradecanediol (mmol)	Oleylamine (mmol)	Oleic Acid (mmol)	Benzyl Ether (mL)	Phenyl Ether (mL)	1-Octadecene (mL)
4	10	--	6	6	--	20	--
5	10	--	12	12	20	--	--
6	10	--	6	6	20	--	--
7	10	--	12	12	15	--	--
8	10	--	12	12	10	--	--
8	10	--	6	6	15	--	--
8	--	10	6	6	20	--	--
~9	10	--	4	4	15	--	--
~9	10	--	4	4	20	--	--
11	--	--	10	--	10	--	--
12	10	--	6	6	--	--	20
~15	10	--	6	6	10	--	--

Not only is the size affected by the changing amounts of solvent and surfactant to metal ratios, but also the shape of the resulting MNPs. For example, when small amounts of solvent are combined with small amounts of surfactant and a shorter alcohol chain, a mixture of triangular and spherical MNPs are obtained. This happens because the growth process of the material was allowed to continue on only certain crystallographic directions of the particle, and terminated in others [16]. The reason we still see some spherical MNPs is because the entire reaction ended earlier for them. This is also why the spherical MNPs are smaller than the triangular ones. Figure 6.5 shows a mixture of triangular and spherical MNPs and star-like MNPs.

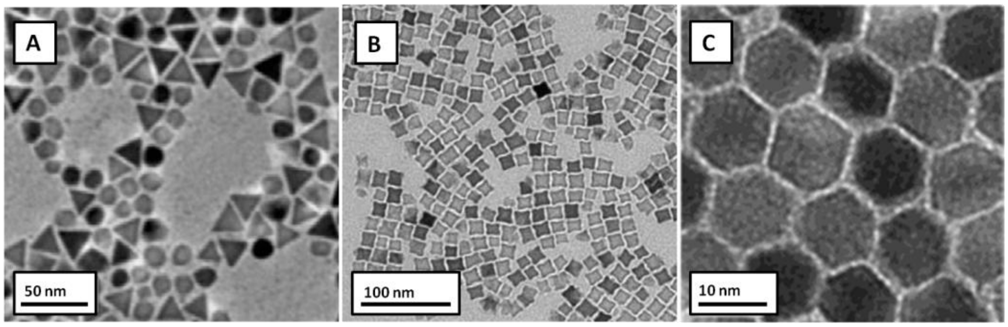

Fig. 6.5. Differently shaped MNPs synthesized via thermal decomposition: (A) Nano triangles and spheres were synthesized using Fe(acac)$_3$, 1,2-tetradecanediol, oleic acid, oleylamine, and 10 mL of benzyl ether; (B) Square/star-like MNPs were synthesized via using Fe(acac)$_3$, 1,2-hexadecanediol, oleylamine, 1-adamantanecarboxylic acid, and 20 mL of benzyl ether; (C) Hexagonal MNPs were synthesized using 1,2-hexadecanediol, oleic acid, oleylamine and 20 mL of benzyl ether. Reprinted with permission from: ***[16]***; Ref. [22]; and Ref. [23]: H. Zeng, P.M. Rice, S.X. Wang, and S. Sun, *Journal of the American Chemical Society* **2004**, *126*, 11458. Copyright 2011 American Chemical Society.

Reducing the reaction time of the synthetic procedure can also change the morphology of the ferrite MNPs. For example, if a synthetic procedure is terminated during the reflux stage, when the particles are re-forming, the MNPs may not have the opportunity to fully form [24].

Figure 6.6 is a perfect example of partially formed MNPs. Here, the MNPs were immediately heated to a reflux temperature of 290°C and were kept there for a short period of time with a small amount of solvent. The resulting particles came out rather large, over 100 nanometers, and had rather non-uniform shape and size, but as further heating was applied to the system with the same initial reactants, the MNPs became more uniform and eventually ~150 nanometer uniform magnetite nanocubes were obtained.

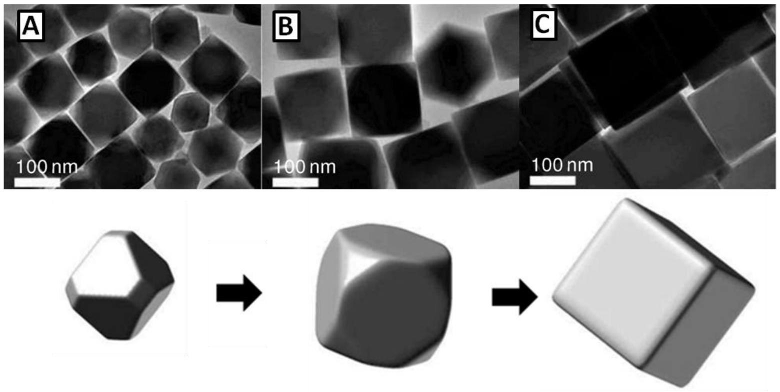

Fig. 6.6. MNPs at different stages of the synthetic procedure. As further heating was applied, the particles grew in size and became more uniform in shape. The flow chart shows a schematic of the growth process for these MNPs. Reprinted with permission from Ref. [24]: D. Kim, N. Lee, M. Park, B. H. Kim, K. An and T. Hyeon, *Journal of the American Chemical Society* **2009**, *131*, 454. Copyright 2011 American Chemical Society.

2.2 Chemical co-precipitation

Chemical co-precipitation is the most commonly used synthetic technique for making ferrite materials. The idea behind chemical co-precipitation is a simple one that many will recall from chemistry class. There is a starting solution containing many materials that are in equilibrium. When a specific material is added to this solution, an instant reaction occurs. As the name implies, the reaction splits the solution into a supernatant and a precipitate. With this synthetic procedure, the precipitate consists of MNPs.

This is a quick method that can be used to make several different types of materials with excellent phase and shape uniformity, but with poor size-control [9,25-26]. The method for making magnetite MNPs, for example, is combining ferrous (Fe^{2+}) and ferric (Fe^{3+}) salts with an acidic material and precipitating the desired particles with a very alkaline material [25]. The ferrous and ferric salts are generally iron chlorides, sulfates or nitrates. Hydrochloric acid is one example of an acid used for this procedure [9]. Water is also used often as the carrier solvent for the salts during the reaction. Ammonia and sodium hydroxide are frequently used as the base because of their strong alkaline nature. The reaction can be allowed to take place at room temperature or an elevated temperature in an inert atmosphere.

Once all of the precipitate has formed, the reaction is finished and it is vital to wash the MNPs. The resulting MNPs are washed by centrifugation in the presence of ethanol and water to remove any unreacted chemicals from the final product. Figure 6.7 shows a cartoon of the mechanism behind the chemical co-precipitation synthetic route.

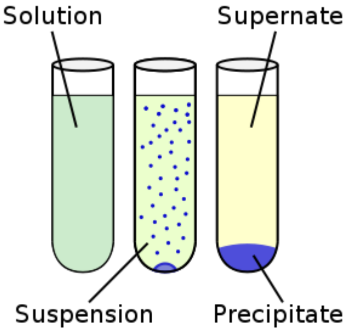

Fig. 6.7. This cartoon illustrates the basic idea behind the mechanics to the chemical co-precipitation technique. Start off with a solution containing suspended materials, add a reactant, and end up with a supernatant and a precipitate where the precipitate is generally the desired material.

Unlike with the thermal decomposition synthetic route, surfactants are often added after the chemical co-precipitation synthetic procedure is finished. This must be done carefully because ferrite MNPs can easily be oxidized. For example, magnetite MNPs can be easily oxidized to maghemite (γ-Fe_2O_3) when exposed to ambient conditions. It is possible to add a polymer during or just after the reaction to surface functionalize the MNPs, thus protecting them from further oxidation. For example, it has been reported that surfactants in aqueous solutions, such as sodium oleic acid, dodecylamine, and sodium carboxymethyl cellulose can be added during the chemical co-precipitation procedure. And if one is to add a polymer instead of a surfactant, they could do so during the reaction by having water as the initial carrier solvent along with a polymer, such as polyvinylalcohol (PVA), dissolved in it [26]. The rest of the reaction would then carry on as before and the phase of the MNPs would remain intact.

As mentioned earlier, it is possible to obtain a shape and size variance for ferrite MNPs when conducting chemical co-precipitation. Components that affect size, shape and phase variance of the material include, but are not limited to: ratio of Fe^{2+}/Fe^{3+} salts, pH of the solution, temperature and length of the reaction.

2.3 Solvothermal

The *solvothermal* method differs from thermal decomposition and chemical co-precipitation in the sense that the reaction does not take place in a vessel where one can watch the reaction occur. This synthetic route consists of placing a mixture of metallic precursor solutions with surfactants and solvent into a sealed autoclave to create MNPs by applying pressure [9, 14]. When the solvent is water, this method is called *hydrothermal* synthesis. After the materials are added to the sealed autoclave, the entire setup is placed into a constant temperature vessel, such as a water, oil, or sand bath and heated to an elevated temperature to “pressure cook” the materials. The resulting material is not plentiful; however the resulting particles are typically very uniform in size and shape [9]. Figure 6.8 shows a diagram of the solvothermal synthetic technique.

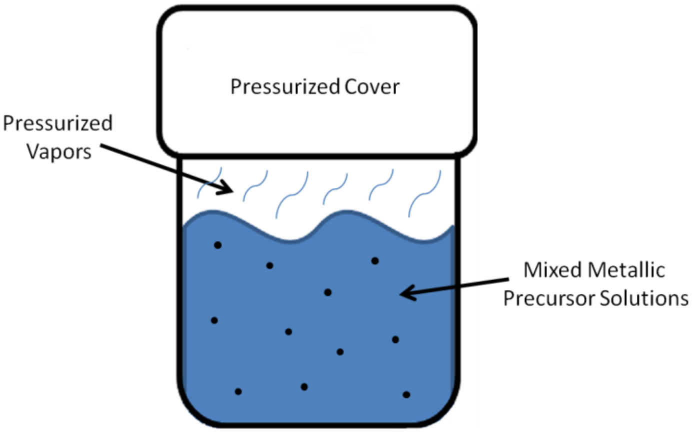

Fig. 6.8. Autoclave that would be suspended in a constant temperature water, oil, or sand bath, depending on the temperature requirements of the reaction. The schematic shows the mixed metallic precursor solutions and the pressurized vapors they create, with MNPs beginning to form from the pressure.

The size and shape of MNPs made by the solvothermal method, as with other techniques discussed, can be controlled by type of solvent used, temperature of the reaction, length of the reaction and ratio of surfactants [14]. Figure 6.9 shows how drastically the shape of MNPs can change with the variance of one surfactant and two examples.

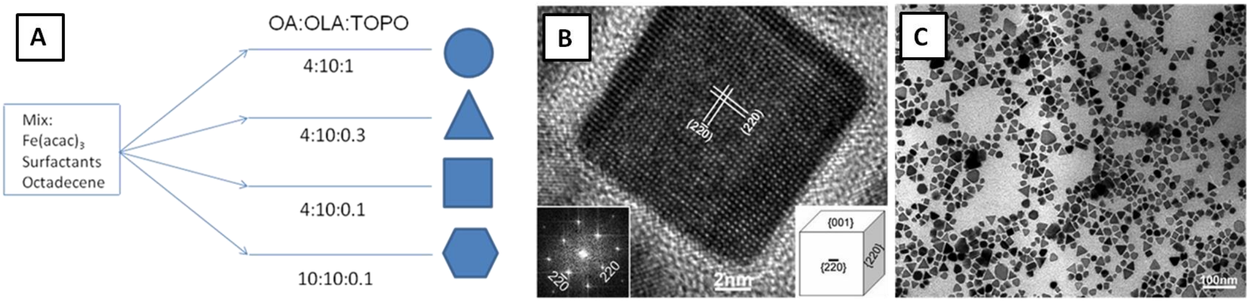

Fig. 6.9. (A) Shape variance with ratio change of the surfactants oleic acid (OA), oleylamine (OLA) and tri-n-octylphosphine oxide (TOPO), in mL; (B) High resolution TEM image of one MNPs showing crystallographic order of the molecules and diffraction pattern; (C) Mixed array of shapes and sizes, primarily triangular made by using the solvothermal route. Reprinted with permission from Ref. [14]: G. Gao, X. Liu, R. Shi, K. Zhou, Y. Shi, R. Ma, E. T. Muromachi

and G. Qiu, *Crystal Growth & Design* **2010**, *10*, 2889. Copyright 2011 American Chemical Society.

2.4 Microemulsion

Microemulsion will be the last discussed synthetic technique for making size and shape-variant ferrites. Synthesis of MNPs by microemulsion is desirable because of the excellent control over shape, size, and phase of resulting MNPs with the relative ease of this technique [9, 27]. The drawback is that only a small amount of product results.

Microemulsion involves the mixing of two immiscible liquids in the presence of metal salts to create the desired particle. There are two types of microemulsion synthetic process possible, water-in-oil and oil-in-water microemulsions [9]. When the two immiscible liquids are mixed together, one forms microdroplets in the other. These microdroplets are stabilized in the solution by surfactants; hence the surfactant plays a crucial role in this synthetic technique, acting as a stabilizing agent for the entire solution rather than just the resulting MNPs. The *surfactant film* is the boundary between the microdroplets and the encompassing solution [27]. With a water-in-oil microemulsion, the microdroplets are called *reverse micelles* because the hydrophilic head of the surfactant faces the center. With an oil-in-water microemulsion, the microdroplets are appropriately called *micelles*, with the hydrophilic head of the surfactant facing out, towards the water. The size of the micelles or reverse micelles is determined by the water-to-oil ratio within the vessel. In MNP synthesis, water-in-oil microemulsions, or synthesis by reverse micelle, are more popular than oil-in-water microemulsions.

To create ferrite MNPs, two separate water-in-oil microemulsions are required [9,27]. The reverse micelles contain the necessary reactants to form the desired MNPs. The two microemulsions are then mixed together with collisions between the two types of reverse micelle occurring. The droplets are dominated by Brownian motion because of their small size and rarely remain stuck together. This collision and separation process creates nucleation and growth of MNPs in the form of a precipitate within the reverse micelles. This precipitate contains the desired MNPs as shown in Fig. 6.10A.

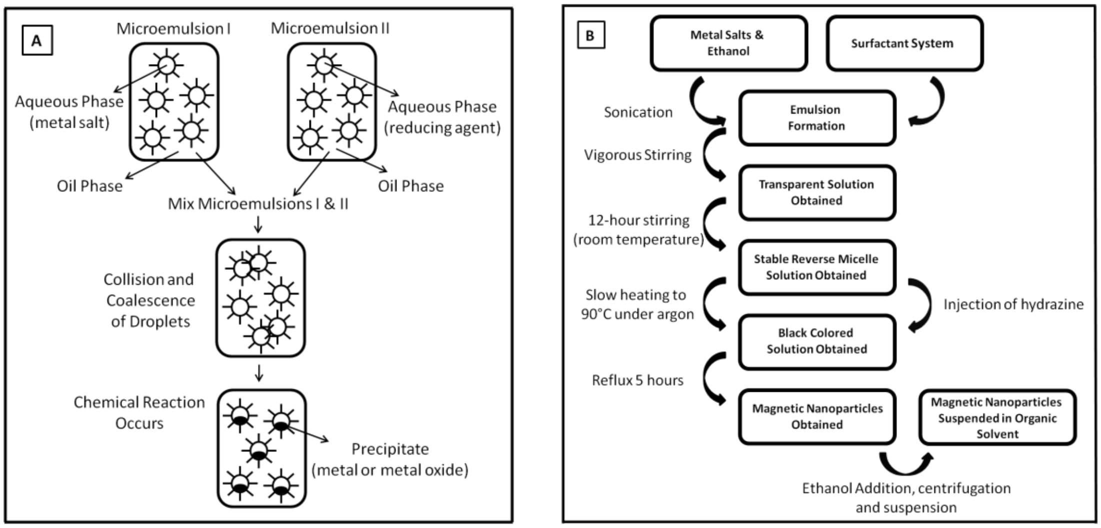

Fig. 6.10. (A) Schematic showing the basics of how the microemulsion synthetic technique works; (B) More detailed flow chart outlining specifically how ferrite MNPs are made using microemulsions. Reprinted with permission from Ref. [27].

As detailed in Fig. 6.10B, the two microemulsions are sonicated after combination to create one coherent microemulsion, which is then vigorously stirred until a transparent solution is obtained. The solution is stirred for several hours at room temperature until stable. At this point, slow heating under an inert gas takes place until the precipitate is formed, and the solution is left to reflux at full temperature until the reaction ends. Finally the MNPs are centrifuged to remove any undesired chemicals and the resulting MNPs can be suspended in an organic solvent.

There are many ways in which one can change the MNP size in microemulsions and keep a uniform particle size distribution [27]. One way to change the MNP size is to alter the reactant concentration within the first microemulsion. More reactant to less carrier solvent will yield larger MNPs. Increasing the flexibility of the surfactant-film will also create larger MNPs. Increasing the film flexibility can be done by adding an alcohol as a co-surfactant or decreasing the molecular weight of the carrier oil in the microemulsion. The final way to increase MNPs size in the microemulsion technique is by increasing the droplet size of the microemulsions in the combined solution. To decrease the size of the MNPs, one can increase the concentration of one reactant far beyond that of the other. This would mean that there is less material overall to react, and thus smaller particles would be created, however more reagents would be wasted in the process.

3. Other magnetic nanoparticles: synthesis of size- and shape-variance

Up until this point, only ferrite MNPs have been discussed, and although magnetite, a ferrite, has already been FDA approved for use in the biomedical field, many other types of MNPs are promising for future use. This section will highlight exciting work being done to synthesize shape and size-variant MNPs other than ferrites [13, 28]. Since thermal decomposition is a moderately easy synthetic route that takes only a few hours with narrow size distribution, very good shape control and a scalable yield of product, it makes sense that this method is very popular for synthesizing MNPs other than ferrites. Figure 6.11 shows images of several differently shaped and sized iron-platinum MNPs synthesized under various conditions using thermal decomposition [13].

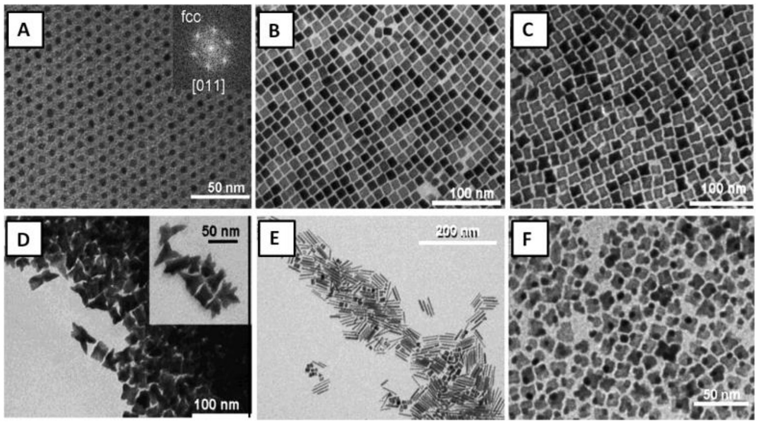

Fig. 6.11. Fe-Pt MNPs of different shapes and sizes using a thermal decomposition synthetic route. Ref. [13]: D. Ung, L.D. Tung, G. Caruntu, D. Delapostas, Y. Alexandrous, I. Prior and N.T.K. Thanh, *CrystEngComm* **2009**, *11*, 1309. Reproduced by permission of The Royal Society of Chemistry.

Table 6.2 shows size and shape of iron-platinum, iron-palladium, and iron-platinum-palladium alloys alongside the amount and type of reagents used. It is obvious to see that a wide variety of shapes and sizes are available ranging from spheres, to cubes, to stars and octopods. The differently shaped MNPs are especially promising for biomedical applications such as cell tagging and targeted drug delivery among other things, as will be discussed later in this chapter.

Table 6.2. Various size and shape trends along with amounts and type of reagents used to make Fe-Pt and Fe-Pd alloys. $Fe(CO)_5$ stands for iron pentacarbonyl, $Pt(acac)_2$ stands for platinum (II) acetylacetonate, $Pd(OA)_2$ stands for palladium (II) acetate, OLA stands for oleylamine, OA stands for oleic acid, MA stands for myristic acid, and HDA stands for hexadecylamine [13].

Size (nm)	**Shape**	**$Fe(CO)_5$ (mmol)**	**$Pt(acac)_2$ (mmol)**	**$Pd(OAc)_2$ (mmol**	**$Pd(acac)_2$ (mmol)**	**OLA (mmol)**	**OA (mmol)**	**MA (mmol)**	**HDA (mmol)**
5±0.6	Spherical-fcc	8.3	8.3	--	--	433	--	--	--
5-50	Mixed	8.3	8.3	--	--	--	433	--	--
Varied	Cube-like	8.3	8.3	--	--	--	--	266	266
9.8±1.6	Cubes	8.3	8.3	--	--	466	466	--	--
13.2±2	Octopod-cubic	8.3	8.3	--	--	466	466	--	--
24.2±6.1	Stars	6.25	6.25	--	--	--	--	--	--
7.5±1	Cubes	8.3	8.3	--	--	--	--	--	--
8.7±1.5	Cubes	16.6	8.3	--	--	--	--	--	--

7.6±1.2	Cubes	24.9	8.3	--	--	--	--	--	--
12.5±2	Mixed	83	8.3	--	--	--	--	--	--
15-20	Tetrahedral	8.3	--	8.3	--	133	133	--	--
13-17	Tetrahedral	8.3	--	8.3	--	--	--	133	133
--	Multipod	8.3	--	--	8.3	--	--	--	--

4. Magnetism in ferrite nanoparticles

The magnetic properties of ferrite MNPs are size and shape dependent. In order to effectively use ferrite MNPs for biomedical applications, a clear understanding of the size- and shape-dependent magnetic properties of these MNPs is needed. The following parts are devoted to achieving this goal.

4.1 Crystal structure and spin configuration

Ferrimagnetic oxides of AB_2O_4 crystallize either in a normal spinel structure or in an inverse spinel structure. In a normal spinel structure, the A^{2+} cations occupy the tetrahedral sites whereas the B^{3+} cations occupy the octahedral sites (Fig. 6.12a). However, in an inverse spinel structure, half of the octahedral coordination sites are occupied by A^{2+} cations and the remaining half as well as all the tetrahedral coordination sites are occupied by the B^{3+} cations. For example, Fe_3O_4 (magnetite) has a normal (cubic) spinel structure with oxygen anions forming a face-centered-cubic (fcc) closed packing and iron (cations) located at the interstitial tetrahedral sites (T_d) and octahedral sites (O_h). The cubic unit cell has lattice parameter a = 8.39 Å [29]. The magnetic moments of both Fe^{2+} and Fe^{3+} cations at the octahedral sites are aligned parallel to an external magnetic field, whereas those of Fe^{3+} ions at the tetrahedral sites are aligned antiparallel to the external magnetic field (Fig. 6.12b).

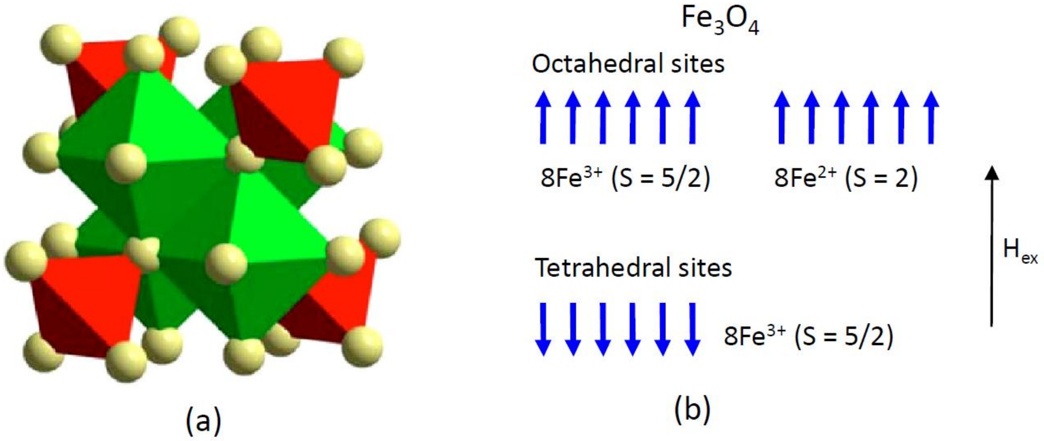

(a) (b)

Fig. 6.12. (a) The crystal structure of an AB_2O_4 spinel. The A-sites ions (red) are embedded in a tetrahedral environment of oxygen (yellow), while the B sites (green) have octahedral environment; (b) The spin configuration of Fe_3O_4 in an applied external magnetic field (H_{ex}).

Since Fe^{2+} has a d^6 electron configuration with a high spin state and Fe^{3+} has d^5 electron configuration with a high spin state, the total magnetic moment of the unit cell of Fe_3O_4 comes only from Fe^{2+} cations with a magnetic moment of 4 μ_B. As Fe is partially substituted by M (M = Co, Ni, and Mn) ferrimagnetic oxides with distinct magnetic properties such as $CoFe_2O_4$, $NiFe_2O_4$, and $MnFe_2O_4$ are created [2,3]. As an example, $CoFe_2O_4$ (cobalt ferrite) is a well-known hard magnetic material with high degree of magnetic anisotropy and magnetostriction [30]. The Co^{2+} and Fe^{3+} cations locate on the octahedral and tetrahedral sites, respectively, forming an inverse spinel structure. The cubic unit cell has lattice parameter (a_o) of 8.39 Å. Since the 8 Fe^{3+} ions in the tetrahedral sites are aligned antiferromagnetically with respect to the 8 Fe^{3+} ions in the octahedral sites via super-exchange interactions mediated by oxygen ions. As a result, the uncompensated Co^{2+} ions possessing three unpaired electrons in their *d*-orbitals would give a theoretical saturated magnetization value of 3 μ_B per unit cell. It has been experimentally shown that the total magnetic moment increases to 5 μ_B for $MnFe_2O_4$ as Fe is partially substituted by Mn, while it decreases to 3 μ_B for $CoFe_2O_4$ and 2 μ_B for $NiFe_2O_4$ as Fe is partially substituted by

Co and Ni, respectively [31]. For biomedical applications, MNPs having large magnetic moments are often preferable [32]. This is why $MnFe_2O_4$ MNPs are being widely used for enhancing magnetic resonance (MR) signals *in vivo* detection of biological targets [4].

4.2. Critical size and superparamagnetism

Refinement of particles size in magnetic materials is essential for obtaining desired magnetic properties. It has been shown that reducing ferromagnetic particles down to the nanometer size (below 100 nm) can lead to an appearance of anomalous magnetic properties [33,34]. As a ferromagnetic particle reaches a critical grain size (D_c, the critical diameter), it is a single magnetic domain [34]. As particle size is smaller than D_c, it significantly affects the magnetic properties of the material. The dependence of the particle size on coercivity (H_C) of a magnetic material is illustrated in Fig. 6.13.

Large particles energetically favor the formation of domain walls to form multi-domain (MD). Magnetization reversal occurs via the nucleation and motion of these walls. In this case, the coercivity (H_c) scales as D^{-n}. As the particle size decreases toward a critical particle diameter, D_c, the formation of domain walls becomes energetically unfavorable and the single domain (SD) particles are consequently obtained [33-35]. In this case, the magnetization process occurs mainly via a coherent rotation of magnetic moments, resulting in larger coercivity. As the particle size decreases to the single-domain value D_{sp}, the coercivity varies with the particle size as $H_c \sim D^6$. Below D_{sp}, the magnetic ordering state is easily collapsed due to thermal fluctuations, and the material exhibits a superparamagnetic feature.

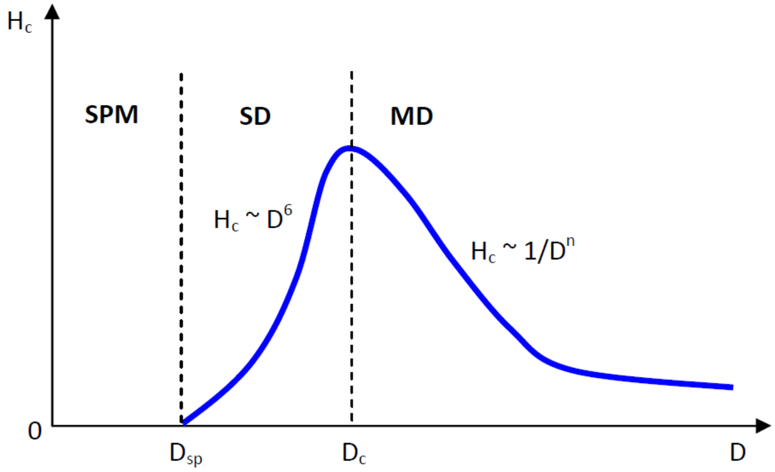

Fig. 6.13. Particle size (*D*) dependence of coercivity (H_c). $H_c = 0$ below the superparamagnetic (SPM) particle size limit D_{sp}, the single domain (SD) particle between D_{sp} and the single-domain limit, D_c and multiple domain (MD) particles.

Furthermore, it has been shown that the critical grain size is dependent on the shape of the particle. For spherical particles with high anisotropy, the critical diameter (D_c) is determined by [34]

$$D_c = \frac{9\gamma}{2\pi M_s^2} \cong 1.44 \frac{\gamma}{M_s^2}, \tag{1}$$

where $\gamma \cong 4\sqrt{AK_1}$ is the specific domain wall energy, A is the exchange constant, and K_1 is the first-order anisotropy constant. It has been found that for $CoFe_2O_4$, Fe_2O_3, Fe_3O_4, FeCo, FePt, CoPt, Ni, and Co spherical particles, the critical diameters are about 100 nm, 91 nm, 82 nm, 52 nm, 56 nm, 58 nm, 84 nm, and 80 nm, respectively [36]. It is worth noting that particles with significant shape anisotropy can remain single domains in much larger dimensions than their spherical counterparts.

4.3. Size-dependent magnetic properties

4.3.1. Static magnetic properties

The magnetic properties of ferrite MNPs are strongly particle-size dependent [37-41]. As an example, Fig. 6.14 shows the temperature dependence of zero-field-cooled (ZFC) and field-cooled (FC) magnetization (e.g. M-T curves) for Fe_3O_4 MNPs with two different sizes of 6 nm and 14 nm. Unless specified, the results presented and discussed in this section are for "spherical" MNP assemblies. It can be seen in Fig. 6.14 that both samples undergo a transition from the ferromagnetic (blocked) state to the superparamagnetic state with increasing temperature. The narrow shape of the ZFC M(T) curve observed for 6 nm Fe_3O_4 MNPs is consistent with the perspective of an assembly of weakly interacting single-domain particles, whereas the broadening of the ZFC M(T) curve observed for 14 nm Fe_3O_4 MNPs points to the system with stronger dipolar inter-particle interactions [42]. It has also been noted that the shape of a ZFC M(T) curve strongly depends on distribution in particle size, with a larger particle size distribution resulting in a broader ZFC M(T) curve [35]. The temperature corresponding to the maximum in the ZFC M(T) curve is referred as to the mean blocking temperature (T_B), which is proportional to the anisotropy constant (K_u) and magnetic volume (V) of the particle via $T_B = K_uV/25k_B$, with k_B is Boltzmann constant.

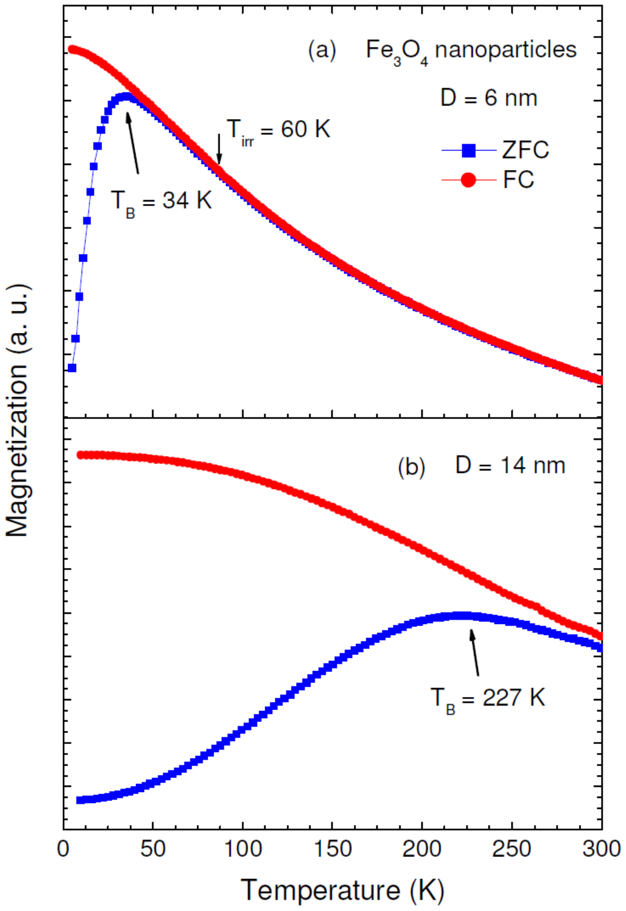

Fig. 6.14. ZFC and FC magnetization versus temperature (M-T) curves of Fe_3O_4 MNPs with two different sizes of (a) 6 nm and (b) 14 nm.

As one can see clearly in Fig. 6.14, the T_B decreases from 227 K to 34 K as the particle size decreases from 14 nm to 6 nm. The decrease of T_B with decrease in particle size represents a general trend for ferrite particle systems (Fig. 6.15). It has also been noted that values of T_B could be varied, depending upon sample synthetic conditions [43] and/or non-stoichiometry [44]. The temperature below which the ZFC and FC curves begin to separate from each other is referred as to the irreversibility temperature (T_{irr}), which is often associated with the blocking of the biggest particles. In this case, a particle system with T_{irr} well far above T_B often shows a large particle size distribution [37-42]. This is true for the case of 14 nm Fe_3O_4 MNPs when compared to that of 6 nm Fe_3O_4 MNPs. Above T_{irr}, the system enters a fully superparamagnetic regime. Another feature to be noted in the FC M(T) curve is that for an assembly of fine particles the continuous increase of the FC magnetization with lowering temperature implies weaker inter-particle interactions. As for Fe_3O_4 material, we recall that while the bulk undergoes a first order magnetic/structural transition (the well-known Verwey transition) at T_v ~115 K, this transition temperature is largely shifted to a lower value in MNP systems, as particle size is decreased below 50 nm (T_v ~ 16 K) [29].

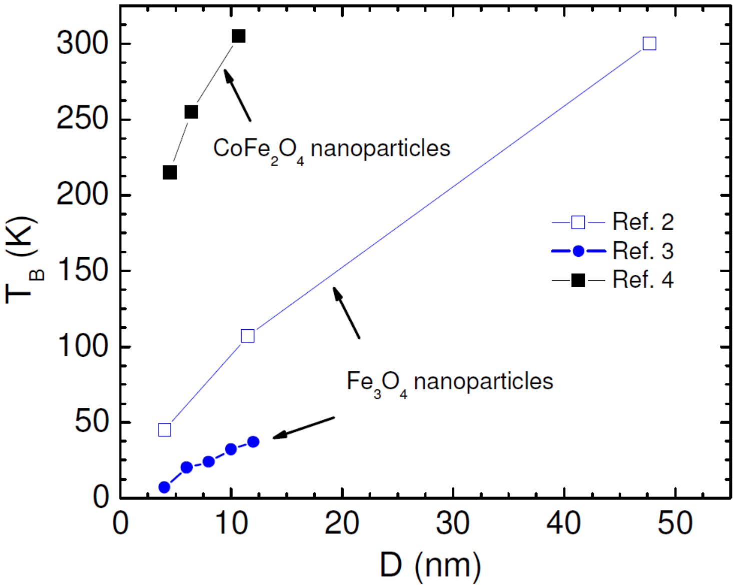

Fig. 6.15. Particle size dependence of the blocking temperature (T_B) of Fe_3O_4 and $CoFe_2O_4$ MNP systems.

Figure 6.16 shows the magnetic field dependence of magnetization (the M-H curves) taken at 10 K and 300 K for 6 nm Fe_3O_4 MNPs. The M-H curves at 300 K do not show any hysteresis, whereas a clear hysteresis with a coercivity of H_C ~223 Oe is observed at 10 K. This is characteristic of the sample being superparamagnetic at room temperature and entering a blocked state at low temperature which results in opening up of the hysteresis loop.

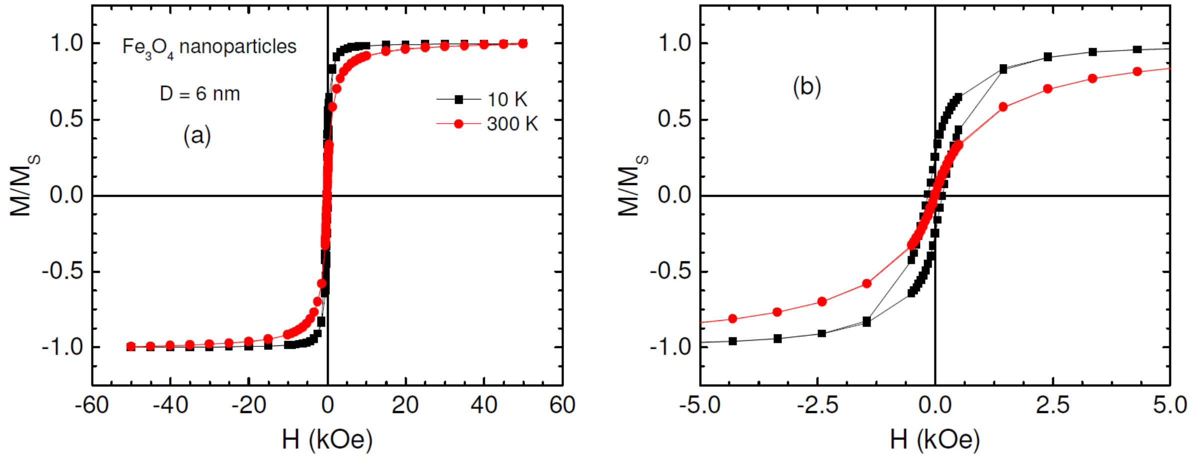

Fig. 6.16. Magnetic hysteresis loops of 6 nm Fe_3O_4 MNPs: (a) full loops and (b) enlarged loops.

In the superparamagnetic regime, the magnetization M(T,H) of a non-interacting, single domain particle can be described by the Langevin relation [29]:

$$M(T,H) = N\mu L\left(\frac{\mu H}{k_B T}\right) = N\mu\left[\coth\left(\frac{\mu H}{k_B T}\right) - \left(\frac{k_B T}{\mu H}\right)\right], \tag{2}$$

where $M_s = N\mu$ is the saturation magnetization resulting from N particles with magnetic moment μ. L(x) is the Langevin function with $x = \mu H/k_B T$ being the magnetic to thermal energy ratio. In the case of a MNP assembly with particle size distribution, the magnetization of the system is modified from Eq. 2 to include the distribution profile:

$$M(T,H) = N\int_0^\infty \mu L\left(\frac{\mu H}{k_B T}\right) f(\mu)d\mu \tag{3}$$

with $f(\mu) = \frac{1}{\sqrt{2\pi}\sigma_\mu \mu}\exp\left\{\frac{\ln^2[\mu/\langle\mu\rangle]}{2\sigma_\mu^2}\right\}$.

From fitting the 300 K M-H data to Eq. 2 for the case of 6 nm Fe_3O_4 MNPs (Fig. 6.17), we have obtained $\mu = 6705\ \mu_B$. This value is close to that reported for 6.7 nm Fe_3O_4 MNPs ($\mu = 6599\ \mu_B$) by Goya *et al.* [29]. Depending on the size and material, the magnetic moments of single-domain particles can vary between 10^3 and 10^5 μ_B [34].

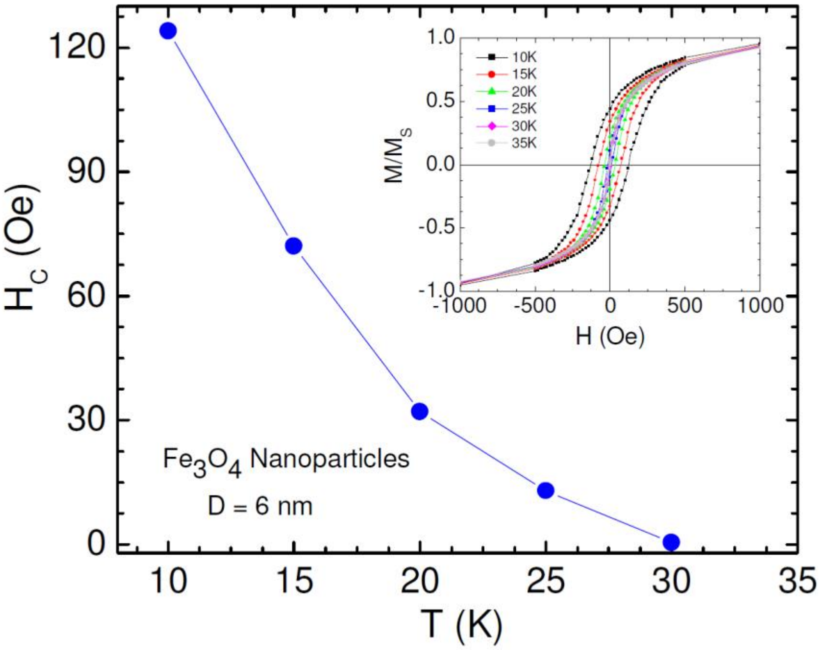

Fig. 6.17. Temperature dependence of coercivity (H_C) of 6 nm Fe_3O_4 MNPs. Inset shows the magnetic field dependence of normalized magnetization (M/M_S) at $T < T_B$.

In the ferromagnetic (blocked) state ($T < T_B$), the saturation magnetization (M_S) increases and the coercivity (H_C) decreases as temperature decreases (Fig. 6.17 and its inset). If a system consists of non-interacting single-domain particles, the temperature dependence of H_C, as extracted from the M-H curves, follows the relation [45]:

$$H_C = H_{CO}\left[1-\left(\frac{T}{T_B}\right)^{\frac{1}{2}}\right], \qquad (4)$$

where $T_B = K_uV/25k_B$ and $H_{co} = 2\alpha K_u/M_S$ with $\alpha = 0.48$ being a phenomenological constant. By fitting the $H_C(T)$ data (Fig. 6.16) to Eq. 4, we have determined T_B ~35 K and H_{CO} ~100 Oe for 6nm Fe_3O_4 MNPs. Using the obtained values of T_B and H_{CO} and their relationship with K_u, the effective anisotropy is determined to be K_u ~21.5x10^4 erg/cm^3. This value of K_u is close to that of bulk Fe_3O_4 (K_u~18.7x10^4 erg/cm^3), suggesting that magnetocrystalline anisotropy is important and other contribution such as surface anisotropy to the total anisotropy is small in these 6 nm Fe_3O_4 particles.

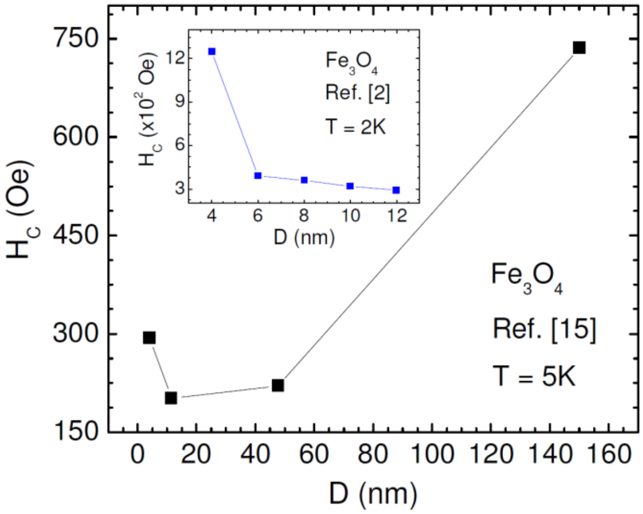

Fig. 6.18. Particle size dependence of coercivity (H_C) of Fe_3O_4 MNPs.

Figure 6.18 illustrates the particle-size dependence of H_C for Fe_3O_4 MNP assemblies. Goya *et al.* [29] reported that with decreasing particle size from 150 nm to 4 nm, the H_C first decreased from 150 nm to 11.5 nm but increased sharply for the smallest particles (D = 4 nm). Dutta *et al.* [37] observed a slight increase in H_C as particle size was decreased from 12 nm to 6 nm and a sudden increase for 4 nm Fe_3O_4 MNPs. In both cases, the strong increase of H_C (Fig. 6.18) for 4 nm Fe_3O_4 MNPs is associated with the strong decrease of M_S (Fig. 6.19), both of which pointed to a strong surface spin disorder that is present in these MNPs.

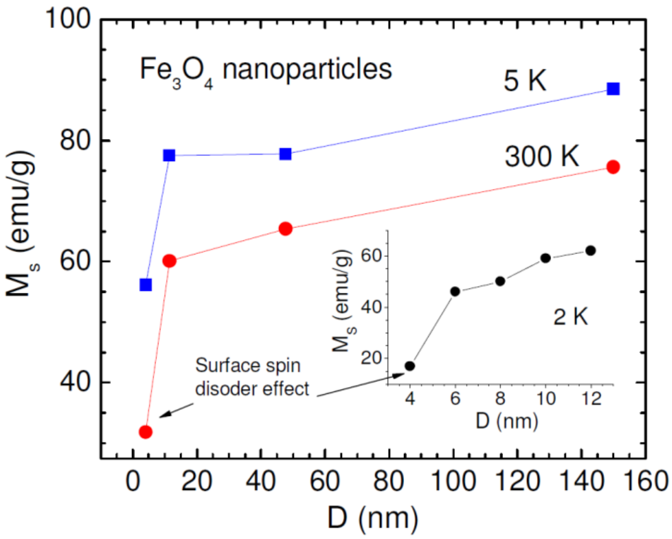

Fig. 6.19. Particle size dependence of saturation magnetization (M_S) of Fe_3O_4 MNPs. The sharp decrease of M_S for 4 nm MNPs is associated with strong surface spin disorder.

It has been suggested that when a large enough fraction of atoms reside at the surface of a particle, the broken exchange bonds are sufficient to induce surface spin disorder thus creating a core-shell structure made of the ferrite core with a shell of disordered spins [46,47]. The fraction of spins on the surface of MNPs increases with decrease in particle size. By assuming a core-shell structure with a shell of thickness d (i.e. the magnetic dead layer) that does not contribute to the saturation magnetization M_S, the variation of M_S with particle size D can be expressed by [37]

$$M_s = M_0(1-2d/D)^3, \tag{5}$$

where M_0 is the saturation magnetization of the bulk. Using this relationship Dutta *et al.* [37] determined the thickness of the spin-disordered shell to be d = 0.68 nm for Fe_3O_4 MNPs with D > 4 nm and d = 0.86 nm for Fe_3O_4 MNPs with D = 4 nm. The remarkable increase in d for Fe_3O_4 MNPs with D = 4 nm gives a natural explanation for the strong decrease in M_S (Fig. 6.19) and the strong increase in H_C (Fig. 6.18).

The high surface-to-volume ratio of 4 nm MNPs resulting in a “shell” of disordered surface spins has also been shown to be responsible for inducing exchange bias (EB) [37]. A Monte Carlo simulation study has recently revealed the possible occurrence of EB in spherical Fe_3O_4 MNPs with mean particle size less than 2.5 nm, where the surface anisotropy (K_s) resulting from disordered surface spins is assumed to be much larger compared to the core cubic magnetocrystalline anisotropy (K_v) [48]. An explanation for the observed EB behavior is that the disordered spins can take on a number of configurations, one of which can be chosen by field-cooling the particle to induce an EB effect [47]. It is believed that the lowest energy configuration of surface spins in the zero-field cooled condition of a spherical particle is the one in which the spins point in the radial direction from the particle [6, 10]. The energy required to rotate these spins contributes to the enhanced coercivity below the spin freezing temperatures as well as “open”, irreversible hysteresis up to high fields [46-50]. The EB has also been observed in $NiFe_2O_4$ [46], $CoFe_2O_4$ [49], and γ-Fe_2O_3 [50] MNPs. Note that the critical size below which the EB appears to occur depends not only on the magnetic nature of MNPs but also on sample processing conditions [34]. Although experimental studies have provided some evidence of surface spin disorder and EB in ferrite MNP systems [51], the physical origins of the surface spin configuration and EB in these systems remain under discussion [47,49]. Another issue of potential interest is if the surface spin alignment in MNPs could be influenced by forming interfaces with other materials [52]. If this is indeed possible, then it would provide an excellent mechanism to control the exchange coupling between the surface and core spins in individual MNPs leading to novel magnetic properties.

4.3.2. Dynamic magnetic properties

AC susceptibility measurements and analyses give important clues about the spin dynamics and the role of dipolar inter-particle interactions between MNPs forming clusters or arrays [33,34,42,53]. In such a MNP system, both real (χ') and imaginary (χ'') components of the AC susceptibility exhibit a frequency-dependent cusp at the spin freezing temperature T_f (T_f is actually T_B as measurement frequency is small). T_f shifts to a higher temperature as measurement frequency (f) is increased (Fig. 6.20, for example, for 6 nm Fe_3O_4 MNPs). With increasing f, χ' decreases while χ'' increases in intensity.

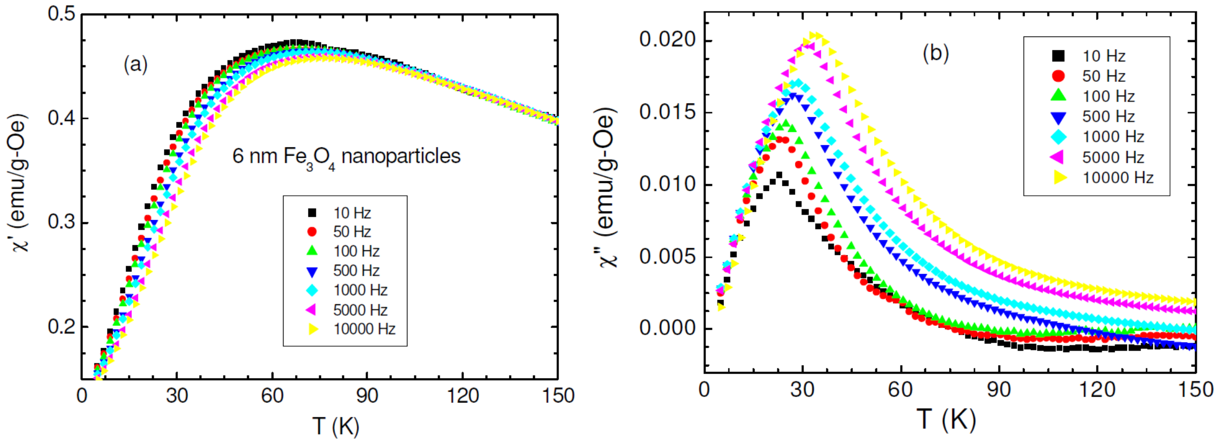

Fig. 6.20. Temperature dependence of (a) the real component and (b) the imaginary component of AC susceptibility at various frequencies 10 Hz – 10 kHz for 6 nm Fe_3O_4 MNPs.

A qualitative and quantitative study of the frequency dependence of χ'or χ'' can help in understanding the spin dynamics better. A useful criterion for classifying the blocking process in an assembly of MNPs can be assessed by the empirical parameter $\Phi = \Delta T_f/[T_f\Delta\log_{10}(f)]$, which represents a fractional change in T_f per decade change in f [29]. For spin glasses Φ is very small (0.005-0.05) and $\Phi \geq 0.13$ for superparamagnetic MNPs. For intermediate values of Φ ($0.05 < \Phi < 0.13$), interparticle interaction is present with its effect decreasing with increase in Φ. Using this criterion, we have obtained $\Phi = 0.08$ for 6 nm Fe_3O_4 MNPs characterizing for an assembly of non-interacting particles and Φ = 0.12 for 9 nm Fe_3O_4 MNPs implying weakly dipolar interparticle interactions that are present in these MNPs.

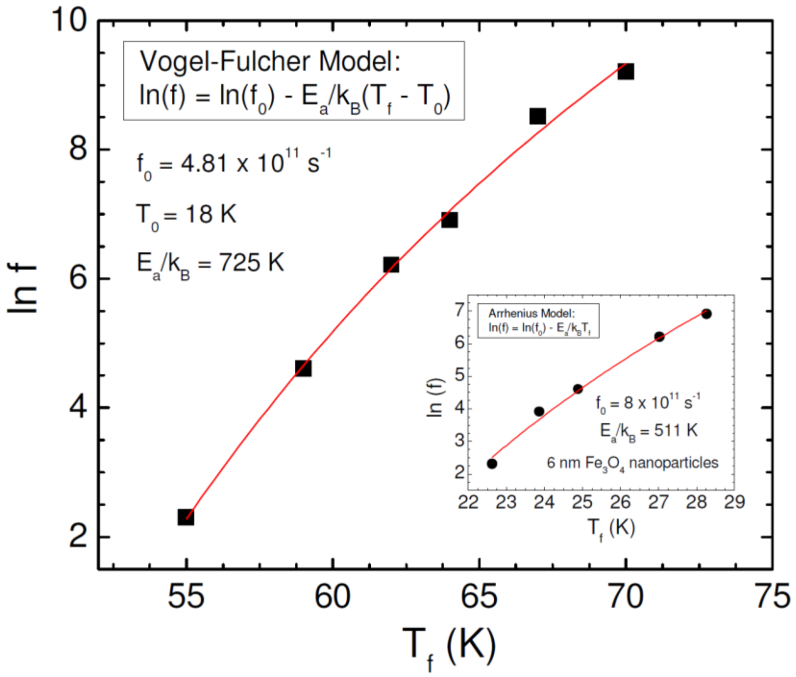

Fig. 6.21. The best fit of $T_f(f)$ data to the Vogel-Fulcher model extracted from χ'' susceptibility of 9 nm Fe_3O_4 MNPs. The inset shows the best fit of $T_f(f)$ data to the Arrhenius model extracted from χ'' susceptibility of 6 nm Fe_3O_4 MNPs.

For a non-interacting MNP system, the frequency dependence of the spin freezing temperature T_f is predicted to follow a simple Arrhenius relation [34]:

$$\tau = \tau_0 \exp\left[\frac{E_a}{k_B T_f}\right] \tag{6}$$

where τ is the relaxation time (τ = 1/f; f is the frequency), τ_o is the microscopic flipping time of the fluctuating spins, E_a is the activation energy barrier that separates the two equilibrium magnetization orientations of the MNPs and k_B is the Boltzmann constant. In the case of superparamagnetic NPs, T_f is identified with T_B. For magnetically interacting MNP systems, the frequency dependence of T_f is better represented by the Vogel-Fulcher relation:

$$\tau = \tau_0 \exp\left[\frac{E_a}{k_B(T_f - T_0)}\right], \tag{7}$$

where T_o is the characteristic temperature with thermal energy dominating for $T > T_o$ and interaction energy for $T < T_o$. Eq. (7) can also be rewritten in the other form, $T_B = T_0 + (E_a/k_B)/\ln(\tau/\tau_0)$. From this equation, it is evident that the magnitude of T_0 is a measure of the strength of the dipolar interparticle interaction and that the larger value of T_0, the larger value of T_B. The best fit of $T_f(f)$ data to the Vogel-Fulcher model extracted from $\chi''(T)$ of 9 nm Fe_3O_4 MNPs yielded $\tau_o = 0.2 \times 10^{-11}$ s, $T_o = 18$ K and $E_a/k_B = 725$ K (Fig. 6.21). This suggests the presence of weakly dipolar interparticle interactions in this system. For 6 nm Fe_3O_4 MNPs, the best fit to the Arrhenius model yielded $\tau_o = 0.125 \times 10^{-11}$ s and $E_a/k_B = 511$ K, suggesting that this system is not magnetically interacting. Goya *et al.* [29] fitted the $\chi''(T)$ data of 5 nm Fe_3O_4 MNPs using the Arrhenius model and yielded $\tau_o = 0.9 \times 10^{-12}$ s for this system. In the limit of superparamagnetic systems, τ_o decreases with decreasing particle size [34]. In the case of interacting MNP assemblies, both τ_o and T_o increase with increasing particle size. We note that both Vogel-Fulcher and Arrhenius models are useful for investigating the relaxation processes in non-interacting and weakly interacting MNP assemblies, but may not be appropriate for studying the spin dynamics of complex composite MNP systems such as Au-Fe_3O_4 nanoclusters [54], in which other types of interaction are dominant over dipolar interparticle interactions.

4.4 Shape-dependent magnetic properties

One of the important sources of magnetic anisotropy comes from the shape of the material. It has been noted that a uniformly magnetized single domain "spherical" particle has no shape anisotropy [34]. However, shape anisotropy is non-zero in a non-spherical particle and it has a significant impact on the magnetic properties of the particle, as the magnitude of the shape anisotropy is dependent on the saturation magnetization. It has also been shown that in large sized particles, shape anisotropy is less important than magnetocrystalline anisotropy [29,34,55]. While the size-dependent magnetic properties of "spherical" ferrite MNPs have been extensively studied in the literature [29,37-41], only a few, incomplete studies have reported on the shape-dependent magnetic properties of ferrite MNPs [14,41,56], probably due to the difficulty in sample synthesis and different processing conditions [2,6,14,57]. For example, Gao *et al.* [14] reported that for Fe_3O_4 nanocubes of 12 nm size the T_B is 81 K and the M_S is 60.3 emu/g. This value of T_B is larger compared to that (38 K) reported by Dutta *et al.* [37] but is much smaller compared with that (T_B ~107 K) reported by Goya *et al.* [29] for 12 nm spherical Fe_3O_4 MNPs. When comparing the T_B, M_s and H_c values between the spherical and cubic $CoFe_2O_4$ nanocrystals over the same magnetic volume, Song and Zhang have shown that while the T_B and M_s are almost the same for both cases, the H_c is significantly larger for the spherical nanocrystals than for the cubic nanocrystals (see Fig. 6.22) [41]. The remarkable difference in H_c between the equal volume spherical and cubic nanocrystals points to the fact that a simple Stoner-Wohlfath theory model cannot fully resolve the fundamental issues in magnetic hysteresis of nanocrystals, as it predicts that H_c of a nanosized material depends on both K_u and M_s via the relation, $H_c = 2K_u/\mu_0 M_s$. The authors have argued that shape anisotropy has a negligible influence in cubic nanocrystals, since a cubic morphology with an aspect ratio of almost 1 is magnetically quasi-isotropic. In this case, surface anisotropy resulting from surface spin disorder and pinning could play a dominant role. When the coordination of surface metal cations has a closer similarity to the coordination symmetry of the metal cations in the core of a nanocrystal, the surface anisotropy should be lower. This suggests that the flat surfaces of cubic nanocrystals should possess a more symmetric coordination and fewer missing coordinating oxygen atoms with respect to the curved topology of spherical nanocrystals [41,56]. As a result, the surface anisotropy and hence coercivity are smaller in the cubic nanocrystals than in the spherical ones. However, a couple of important and unanswered questions have emerged:

1. *Why is the blocking temperature not affected by surface anisotropy?*
2. *What is the fundamental difference between thermally and magnetically overcoming the anisotropy energy barriers?*

To answer these questions, a systematic study of DC and AC magnetization and transverse susceptibility of spherical and cubic ferrite nanocrystals with size variance must be performed and this would be an interesting subject for future research.

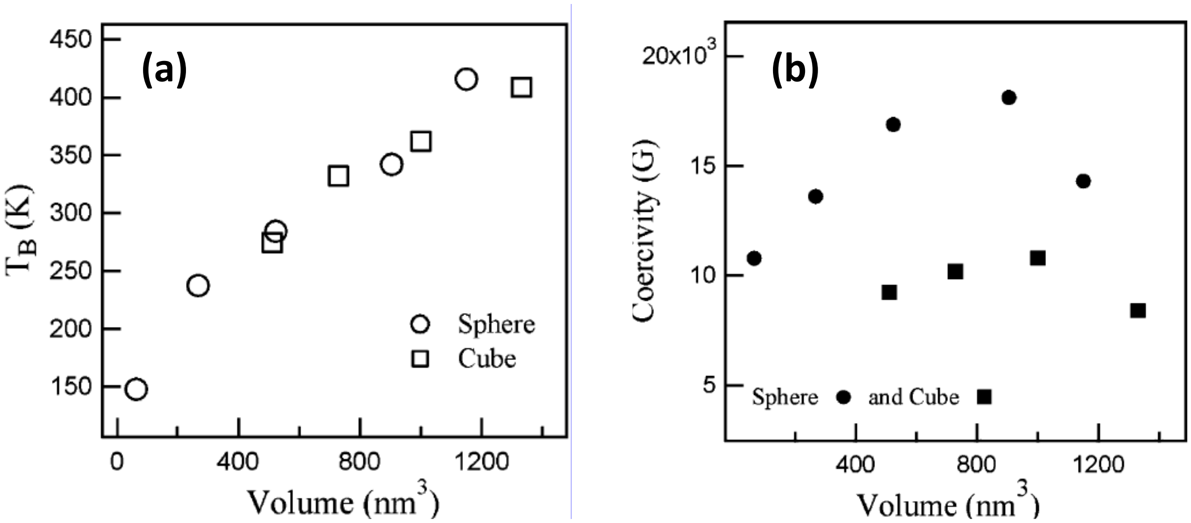

Fig. 6.22. The volume-dependent blocking temperature (a) and coercivity (b) of spherical and cubic $CoFe_2O_4$ nanocrystals. Reprinted with permission from Ref. [41]: Q. Song and Z. J. Zhang, *Journal of the American Chemical Society* **2004**, *126*, 6164. Copyright 2011 American Chemical Society.

Other than ferrite MNPs, shape anisotropy has been shown to play a crucial role in determining the magnetic properties of Co-Pt barcode-structured nanowires with various aspect ratios ($\gamma = b/a$, with *a* and *b* are the diameter and the length of a nanowire, respectively) [36] and

Fe-Pt/Fe-Pd/Fe-Pt-Pd MNPs having different isolated shapes (nanocubes, nanostars, multipods, and bilobars) [13]. In the case of Co-Pt nanowires with $\gamma = 0.25, 1, 3.5$ and 45, the H_c has been found to sharply increase with increasing γ for $\gamma \leq 1$ and then remain almost unchanged for higher γ. Since H_c scales with K_u for $\gamma \leq 1$, the increase of shape anisotropy is expected to increase the H_c in these nanowires. In another study, Ung et al. [13] have observed a gradual increase of T_B of Fe-Pt nanocubes as the particle size increases from 6.7 nm to 13.2 nm. The small values of T_B obtained for these nanocubes could arise from the fact that the nanocubes were crystallized in the disorder fcc phase with low crystalline anisotropy. A noticeable difference in T_B has also been observed by these authors for Fe-Pt nanocrystals with cubic, star, and bilobar shapes [13]. However, the physical origins of the difference in T_B and the role of surface anisotropy remain under discussion. In this context, we propose that a radio-frequency transverse susceptibility (TS) technique based on a sensitive, self-resonant tunnel-diode oscillator would be a very useful tool to resolve different contributions to the effective anisotropy in these MNPs arising from different surface terminations [58].

5. Magnetic nanoparticles for biomedical applications

This section will focus on the inclusion of MNPs in biomedical applications [1,23,59-62]. MNPs are desirable for biomedical use because of their tunable magnetic properties that change with size and shape. Some of the biomedical applications for MNPs include targeted drug delivery, hyperthermia, magnetic resonance imaging (MRI) contrast enhancement, cell tagging, and magnetic separation [1, 59].

5.1 Targeted drug delivery

Targeted drug delivery using MNPs was first proposed in the 1970s [1, 59]. A MNP would be surface functionalized with a drug or medication. Bio-compatible MNPs are injected into the blood stream as part of a ferrofluid and directed to the tumor with an external DC magnetic field. The medication would be on a time-release, set by either enzymatic activity, or determined by other changes such as pH or temperature. MNPs could be surface functionalized so that they would attach to an antibody that would be absorbed by cancer cells, as Figure 6.23 shows [60].

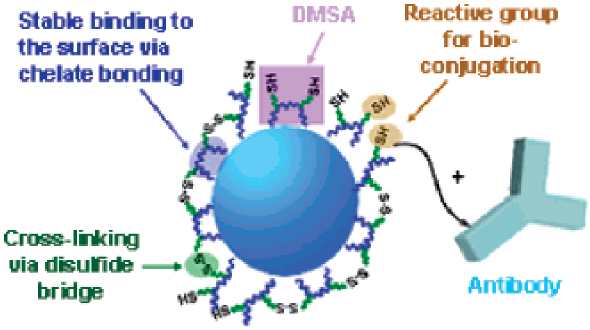

Fig. 6.23. A MNP that has been surface functionalized to attach itself to an antibody that the cancerous cell will absorb. Reprinted with permission from Ref. [60]: Y. W. Jun, Y. M. Huh, J. S. Choi, J. H. Lee, H. T. Song, S. Kim, S. Yoon, K. S. Kim, J. S. Shin, J. S. Suh, and J. Cheon, *Journal of the American Chemical Society*, **2005**, *127*, 5732. Copyright 2011 American Chemical Society.

Targeted drug delivery has been successfully demonstrated on tumors in rats, swine and rabbits. Phase I clinical testing on humans was conducted by infusing surface functionalized magnetic MNPs within a ferrofluid into the patients' blood stream.

5.2 Hyperthermia

Hyperthermia is a procedure in which the body temperature is elevated; this can be used to heat cancer cells above their critical temperature, killing them off and eliminating the cancer without majorly affecting any other part of the body. The first research group to study cancer treatment by hyperthermia was in 1957 by heating 20-100 nm MNPs to using AC magnetic fields with a frequency 1.2MHz [1, 59]. Much like with targeted drug delivery, MNPs would be injected into the bloodstream and directed to the tumor with the aid of an external DC magnetic field. When the MNPs reach the tumor, an AC field is generated and the tumor heats up. If the heat produced can maintain a temperature of 42°C for 30 minutes, the cancer tumor is eliminated. Superparamagnetic MNPs, such as magnetite, have desirable heating features for hyperthermia. Since magnetite MNPs are superparamagnetic, they align under low magnetic fields and would be safer for the patient.

5.3 MRI contrast enhancement

MRI, or *magnetic resonance imaging*, was first introduced in the 1970s as a way to image human body tissues and has since become a staple in the medical field. MRI uses a strong magnetic field (~1-2 Tesla) and radio frequency fields to align magnetic components within atoms in cells [1, 59]. The images received from MRI are able to distinguish irregular tissues, such as tumor tissues, from healthy soft tissues. Although MRI is very good at determining normal from abnormal tissues, contrast enhancement is often needed to make the images more clear. Paramagnetic gadolinium ion complexes are currently used. However, superparamagnetic materials are more desirable for MRI because they saturate under low magnetic fields, indicating that the maximum contrast can be achieved using a safer magnetic field. Figure 6.24 shows the liver of a rat without any enhancement (top) and 12 hours and 45 minutes after Ultra-small superparamagnetic iron oxide (USPIO) enhancement (bottom) [61].

A clinical study of using USPIO on human patients from 2007 examined the images from 9 patients using USPIO as an MRI contrast agent [62]. These patients had either ischemic or hemorrhagic strokes, where there was either a block of blood flow to the brain (ischemic) or an excess of blood to the brain (hemorrhagic). The patients in this study received USPIO infusions between 26 and 96 hours after stroke and had follow-up MRI scans from 1-11 days after infusion. This study determined that the USPIO-enhanced MRI may be of use, specifically when targeting anti-inflammatory therapy in stroke patients.

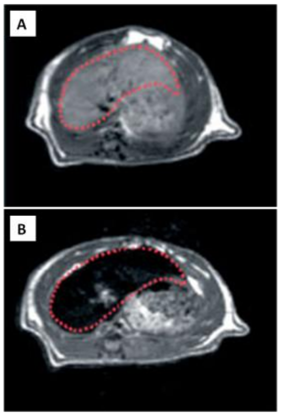

Fig. 6.24. A rat's liver (A) before infusion of USPIO, and (B) 12 hours and 45 minutes after infusion of USPIO. The dark area is where the USPIO has been collected in the liver. Reprinted with permission from Ref. [61].

In these applications, the use of size- and shape-variant MNPs may be advantageous as they have utility in biomedical immune-electron microscopy allowing differentiation by both size and shape simultaneously [13-15]. It has been suggested that MNPs with tunable shapes and sizes can provide more magnetic labeling options that are currently restricted to spherical MNPs below 15 nm in size [13]. As the magnetic easy axis of a particle correlates closely with its crystal structure, the shape-induced crystal orientation of each MNP in an assembly would lead to an aligned magnetic easy axis. This alignment favors a MNP assembly for better use in data storage and biosensing applications [57].

6. Concluding remarks and future directions

This chapter provides an up-to-date review of the currently available chemical methods for synthesis of MNPs with size and shape variance, as well as an important understanding of the size- and shape-dependent magnetic properties of the MNPs. A brief overview of useful biomedical applications using these MNPs is also given.

From the MNPs' synthesis perspective, we recall that thermal decomposition involves decomposing and recombining the initial reagents to obtain a desired MNP. This technique yields excellent control over size distribution and shape of the MNPs based on ratio and types of surfactants, alcohols and solvents. Chemical co-precipitation involves mixing initial reactants and precipitating the desired MNP with addition of a base. This route is decent in terms of size control, but lacking in terms of shape control. The appeal of this technique is that it is quick and simple. Solvothermal or hydrothermal "pressure cooks" the precursor solutions to obtain the desired MNP. The resulting MNPs generally have a very good size distribution and the shape of the MNPs can be changed by altering the ratio and types of surfactants used. The drawback from this technique is that the particle amount is typically rather small and the synthetic procedure cannot be scaled up because of the autoclave. Finally, microemulsion of surfactants and metal precursors are mixed together to create a second microemulsion in which the surfactants and metal precursors join together to create the desired MNP. The size of the MNPs can be easily changed, and the shape control is generally good, however, once again there is a low MNP yield. A summary of these results and trends can be seen in Table 6.3 below.

Table 6.3. Summary of common bottom-up synthetic techniques [9].

Method	Level of Complexity	Conditions	Reaction Temperature (°C)	Reaction Time	Solvent	Surfactants Added	Size Distribution	Shape Control	Yield
Thermal Decomposition	Moderate	Inert atmosphere	100-320	Hours	Organic compound	During reaction	Very narrow	Very good	High-scalable
Co-precipitation	Simple	Inert atmosphere	20-90	Minutes-hours	Water or aqueous solution	During or after reaction	Relatively narrow	Not good	High-scalable
Solvothermal	Complicated	Ambient conditions	100-300	Hours-days	Water or organic solvent	During reaction	Very narrow	Very good	Medium
Microemulsion	Complicated	Ambient conditions	20-50	Hours	Organic compound	During reaction	Very narrow	Good	Low

On the magnetism of the ferrite MNPs, we note that although the size-dependent magnetic properties of the MNPs have been extensively studied to some extent, the physical origins of anomalous magnetic properties at low temperatures, like spin-glass behavior and exchange bias remain to be discussed. While several works were focused mainly on the synthesis of MNPs with shape variance, only a few works reported on the shape-dependent magnetic properties of the MNPs. Noticeably, no work has been found to investigate the dynamic magnetic properties of the shape-variant MNPs. As a result, a complete understanding of the influence of particle shape on the magnetic properties including spin-glass behavior and exchange bias in the MNPs is lacking. This thus warrants future studies.

Magnetic anisotropy plays a key role in controlling the magnetic properties of MNP assemblies. MNP assemblies possess a distribution in the effective anisotropy due to the uniaxial symmetry for spherical particles, distributions in particle size and in their preferred axis directions. While conventional magnetometry cannot resolve some of these features, we propose that a radio-frequency transverse susceptibility (TS) technique based on a sensitive, self-resonant tunnel-diode oscillator can be better suited for this purpose [58,63-65]. In particular, TS would be a very useful tool to resolve different contributions to the effective anisotropy in these nanoparticles arising from different surface terminations [58]. It would also be a very powerful probe of the effect of the strength of the dipolar-dipolar interparticle interactions in MNP assemblies [65]. In these cases, systematic TS studies on MNP systems with size and shape variance should be performed and this would be an interesting subject for future research.

MNPs show great potential for biomedical applications. While MNPs of non-spherical shapes (e.g. triangle, rod, cube, arrow, tetrapod, star, multipods, bilobars, etc.) are expected to provide additional advantages to existing applications, it is unclear how these MNPs can be used as building blocks to control the crystal orientation of the MNPs in an assembly desirable for such applications. Future research should therefore be devoted to addressing this important and emerging issue.

References

1. Q.A. Pankhurst, N.T.K Thanh, S.K. Jones, and J. Dobson, *Journal of Physics D: Applied Physics* **2009**, *42*, 224001

2. A. G. Roca, R. Costo, A. F. Rebolledo, S Veintemillas-Verdaguer, P. Tartaj, T. Gonz´alez-Carreno, M. P. Morales and C. J. Serna, *Journal of Physics D: Applied Physics* **2009**, *42,* 224002.

3. F. Reynolds and J. Zach, *Nanomedicine* **2010**, *5*, 1401.

4. C. Sun, J. S. H. Lee and M. Zhang, *Advanced Drug Delivery Reviews* **2008**, *60*, 1252.

5. J. Llandro, J. J. Palfreyman, A. Ionescu and C. H. W. Barnes, *Medical and Biological Engineering and Computing* **2010**, *48,* 977.

6. C. Xu and S. Sun, *Polymer International* **2007**, *56,* 821.

7. J.A.L. Perez, M.A.L. Quintela, J. Mira, J. Rivas and S.W. Charles, *Journal of Physical Chemistry B* **1997**, *101,* 8045.

8. Y. Lee, J. Lee, C.J. Bae, J.G. Park, H.J. Noh, J. H. Park and T. H. Yeong, *Advanced Functional Materials* **2005***,* *15*, 503.

9. A.H. Lu, E.L. Salabas and F. Schuth, *Angewandte Chemie International Edition* **2007***,* *46*, 1222.

10. S. R. Dave and X. H. Gao, *Nanobiotechnology* **2009**, *1*, 583.

11. I. Robinson, C. Alexander, L. D. Tung, D. G. Fernig and N.T.K. Thanh, *Journal Magnetism and Magnetic Materials* **2009**, *321,* 1421.

12. I. Robinson, M. Volk, L.D. Tung. G. Caruntu, N. Kay and N.T.K. Thanh, *Journal of Physical Chemistry C* **2009**, *113,* 9497.

13. D. Ung, L.D. Tung, G. Caruntu, D. Delapostas, Y. Alexandrous, I. Prior and N.T.K. Thanh, *CrystEngComm.* **2009**, *11,* 1309.

14. G. Gao, X. Liu, R. Shi, K. Zhou, Y. Shi, R. Ma, E. T. Muromachi and G. Qiu, *Crystal Growth & Design* **2010**, *10*, 2889.

15. R. Hao, R. Xing, Z. Xu, Y. Hou, S. Gao and S.H. Sun, *Advanced Materials* **2010**, *22*, 2729.

16. J. Xie, S. Peng, N. Brower, N. Pourmand, S. X. Wang, S. Sun, *Pure and Applied Chemistry* **2006**, *78*, 1003.

17. N.T.K. Thanh, and L.A.W. Green, *Nano Today* **2010**, 5, 213-230.

18. B. L. Frankamp, N. O. Fischer, R. Hong, Sudhandshu Srivastava, and Vincent M. Rotello, *Chemistry of Materials* **2006**, *18*, 956.

19. Y. Wang, J. F. Wong, X. Teng, X. Z. Lin, and H. Yang, *Nano Letters* **2003**, *3*, 1555.

20. J. Xie, C. Xu, N. Kohler, Y. Hou, S. Sun, *Advanced Materials* **2007**, *19*, 3163.

21. T. Pellegrino, L. Manna, S. Kudera, T. Liedl, D. Kiktysh, A. L. Rogach, S. Keller, J. Radler, G. Natile, and W. J. Parak, *Nano Letters* **2004**, *4*, 703.

22. L. Zhang, Y.H. Dou, H.C. Gu, *Journal of Crystal Growth* **2006**, *296*, 221.

23. H. Zeng, P.M. Rice, S.X. Wang, and S. Sun, *Journal of the American Chemical Society* **2004**, *126*, 11458.

24. D. Kim, N. Lee, M. Park, B. H. Kim, K. An and T. Hyeon, *Journal of the American Chemical Society* **2009**, *131*, 454.

25. T. Belin, N. Guigue-Millot, T. Calliot, D. Aymes, and J.C. Niepce, *Journal of Solid State Chemistry* **2002**, *163*, 459.

26. J. Lee, T. Isobe, M. Senna, *Journal of Colloid and Interface Science* **1996**, *177*, 490.

27. D. S. Mathew, R. S. Juang, *Chemical Engineering Journal* **2007**, *129*, 51.

28. N. R. Jana, Y. Chen, X. Peng, *Chemistry of Materials* **2004**, *16*, 3931.

29. G. F. Goya, T. S. Berquó, F. C. Fonseca, and M. P. Morales, *Journal of Applied Physics* **2003**, *94*, 3520.

30. A. Goldman, *Modern Ferrite Technology 2nd Edition*, **2006 (**Springer).

31. Y. W. Jun, J. W. Seo, J.W. Cheon, *Accounts of Chemical Research* **2008**, *41*, 179.

32. T.T. Thuy, S. Maenosono, N.T.K. Thanh, *Magnetic Nanoparticles: From Fabrication to Clinical Applications* **2011** (CRC Press, Taylor and Francis).

33. S. A. Majetich and M. Sachan, *Journal of Physics D: Applied Physics* **2006**, *39*, R407.

34. S. Bedanta and W. Kleemann, *Journal of Physics D: Applied Physics* **2009**, *42*, 013001.

35. A. Labarta, X. Batlle, O. Iglesias, *Surface Effects in Magnetic Nanoparticles* **2006** (Springer).

36. K.M. Krishnan, *IEEE Transactions on Magnetics* **2010**, *46*, 2523.

37. P. Dutta, S. Pal, M. S. Seehra, N. Shah and G. P. Huffman, *Journal of Applied Physics* **2009**, *105*, 07B501.

38. D. Caruntu, G. Caruntu and C. J. O'Connor, *Journal of Physics D: Applied Physics* **2007**, *40*, 5801.

39. H. Iida, K. Takayanagi, T. Nakanishi, T. Osaka, *Journal of Colloid and Interface Science* **2007**, *314*, 274.

40. C.H. Chia, S. Zakaria, M. Yusoff, S.C. Goh, C.Y. Hawa, Sh. Ahmadi , N.M. Huang, H.N. Lim, *Ceramics International* **2010**, *36*, 605.

41. Q. Song and Z. J. Zhang, *Journal of the American Chemical Society* **2004**, *126*, 6164.

42. M. B. Morales, M. H. Phan, S. Pal, N. A. Frey and H. Srikanth, *Journal of Applied Physics* **2009**, *105*, 07B511.

43. H. Yana, J. Zhang, C. You, Z. Song, B. Yu and Y. Shen, *Materials Chemistry and Physics* **2009**, *113*, 46.

44. J. Mazo-Zuluaga, J. Restrepo and J. Mejía-López, *Journal of Physics: Condensed Matter* **2008**, *20*, 195213.

45. E. C. Stoner and E. P. Wohlfarth, *Philosophical Transactions of the Royal Society of London, Series A* **1948**, *240*, 599.

46. R. H. Kodama, A. E. Berkowitz, E. J. McNiff, and S. Foner, *Physical Review Letters* **77**, 394 (1996).

47. O. Iglesias, A. Labarta, and X. Batlle, *Journal of Nanoscience and Nanotechnology* **2008**, *8*, 2761.

48. J. Mazo-Zuluaga, J. Restrepo, F. Muñoz, and J. Mejía-López, *Journal of Applied Physics* **2009**, *105*, 123907.

49. D. Peddos, C. Cannas, G. Piccaluga, E. Agostinelli, and D. Fiorani, *Nanotechnology* **2010**, *21*, 125705.

50. B. Martínez, X. Obradors, Ll. Balcells, A. Rouanet, and C. Monty, *Physical Review Letters* **1998**, *80*, 181.

51. V. Sepelak, I. Bergmann, A. Feldhoff, P. Heitjans, F. Krumeich, D. Menzel, F. J. Litterst, S. J. Campbell and K. D. Becker, *Journal of Physical Chemistry C* **2007**, *111*, 5026.

52. N. A. Frey, S. Sanyadanam, H. Srikanth, C. Wang, and S. Sun, *IEEE Transactions on Magnetics* **2007**, *43*, 3094.

53. S. Pal, S. Chandra, M. H. Phan, P. Mukherjee and H. Srikanth, *Nanotechnology* **2009**, *20*, 485604.

54. N. A. Frey, M. H. Phan, H. Srikanth, S. Srinath, C. Wang and S. Sun, *Journal of Applied Physics* **2009**, *105*, 07B502.

55. T. N. Shendruk, R.D. Desautels, B.W. Southern, and J van Lierop, *Nanotechnology* **2007**, *18*, 455704.

56. N. Z. Bao, L. Shen, P. Padhan, and A. Gupta, *Applied Physics Letters* **2008**, 92, 173101.

57. H. Zeng, P. M. Rice, S. X. Wang, and S. Sun, *Journal of the American Chemical Society* **2004**, 126, 11458.

58. R. Swaminathan, M. McHenry, P. Poddar and H. Srikanth, *Journal of Applied Physics* **2005**, *97*, 10G104.

59. Q. A. Pankhurst, J. Connolly, S. K. Jones and J. Dobson, *Journal of Physics D: Applied Physics* **2003**, *36*, R167.

60. Y. W. Jun, Y. M. Huh, J. S. Choi, J. H. Lee, H. T. Song, S. Kim, S. Yoon, K. S. Kim, J. S. Shin, J. S. Suh, and J. Cheon, *Journal of the American Chemical Society*, **2005**, *127*, 5732.

61. Z. Li, L. Wei, M. Gao, and H. Lei, *Advanced Materials* **2005**, *17*, 1001.

62. A. Saleh, M. Schroeter, A. Ringelstein, H. P. Hartung, M. Siebler, U. Modder, and S. Jander, *Stroke* **2007**, *38*, 2733.

63. H. Srikanth, J. Wiggins and H. Rees, *Review of Scientific Instruments* **1999**, *70*, 3097.

64. P. Poddar, J. L. Wilson, H. Srikanth, D. F. Farrell and S. A. Majetich *Physical Review B* **2003**, *68*, 214409.

65. P. Poddar, M. B. Morales, N. A. Frey, S. A. Morrison, E. E. Carpenter and H. Srikanth, *Journal of Applied Physics* **2008**, *104*, 063901.